ADVANCED OPTICAL MATERIALS
www.advopticalmat.de

All-Optical Polarization-Controlled Nanosensor Switch Based on Guided-Wave Surface Plasmon Resonance via Molecular Overtone Excitations in the Near-Infrared

Alina Karabchevsky, Adir Hazan, and Aliaksei Dubavik*

Semiconductor transistors for sensors are considered the most widely manufactured device in history. Being invented to switch electronic signals they revolutionized electronics and paved the way for smaller and cheaper sensors, radios, calculators, and computers. However, electric switches are hampered by damage from very brief electrical and thermal effects or electromagnetic interference. For this reason, modern communication systems devote considerable attention to all-optical switches, yet, the state-of-the-art switching of photonic signals is fulfilled electronically. All-optical switching allows light-controls-light through unique optical effects. Here, an all-optical sensor switch, engineered to operate at telecommunication wavelengths, caused by the excitation of molecular overtones in a hybrid plasmonic–dielectric configuration is demonstrated. This configuration possesses a unique property: to control the sensor switch with the polarization state of light for two different plasmonic modes to co-exist while exciting a single overtone. Control of the sensor switch is realized by tuning the polarization of incident light from transverse magnetic (switch-on) to transverse electric (switch-off). This switch provides a miniature, affordable, and fast chip-scale polarization-activated sensor device for a wide range of applications from optics communication to all-optical computing and sensing.

1. Introduction

As the field of optical fiber and waveguide technology has expanded,[1,2] optical switches have been studied and have progressed naturally,[3,4] giving rise to new sensing configurations[1] such as optical switching with organics,[5] optically switchable light-emitting transistors,[6] sub-femtojoule switches,[7] plasmonic bandpass filter thermal sensor switches,[8] optical control of antiferromagnetic domains[9] utilizing high-mobility of cadmium oxide for ultrafast polarization-controlled[10] multimodal sensing switching of a redox-active macrocycle molecules state toggle,[11] active control of anapole states by structuring the phase-change alloy,[12] energy-efficient all-optical switching with graphene-loaded deep-subwavelength plasmonic waveguides,[13] and ultrafast optical switching of infrared plasmon polaritons in high-mobility graphene.[14] The efficiency of the switch is defined by its size, which dictates the number of input and output ports; switching time of reconfiguration from one state to another; propagation delay time; switching energy to turn on the switch; power dissipation during the switching; crosstalk due to the power leakage to other ports; and physical dimensions.[3] Even though the optical fibers are considered a pivot of a conventional optic telecommunication system,[2] their role in switching and processing of photonic signals is limited and fulfilled by electronics. Here we report an all-optical switch engineered to operate at telecommunication wavelengths associated with the relaxation time of excited molecules in a hybrid plasmonic–dielectric configuration. By coupling photons to conductive charges at the metal–dielectric interface, plasmonics gives rise to nanoscale optical devices operating at sub-wavelength regime[15] due to the local field enhancement. The local field enhancement can be realized with plasmonic materials by means of collective oscillations of free electrons in the form of extended surface plasmon-polariton (ESP) in thin metal films[16] or localized surface plasmon resonance (LSPR) in plasmonic nanoantennas.[17] However, molecular overtone bands lying in the near-infrared (NIR) spectral region are forbidden in harmonic oscillator approximations.[18–20] Such bands arise only from the anharmonicity of molecular vibrations which are rather weak,[18] leading to overtone bands with the absorption cross-section of an order of magnitude lower than that of the fundamental modes with the same degrees of freedom. Here, we focus on a hybrid plasmonic–dielectric system consisting of excited LSPR of the gold

Dr. A. Karabchevsky, A. Hazan
School of Electrical and Computer Engineering
Electro-Optics and Photonics Engineering Department
Ben-Gurion University of the Negev
Beer-Sheva 8410501, Israel
E-mail: alinak@bgu.ac.il
Dr. A. Karabchevsky
Center for Quantum Information Science and Technology
Ilse Katz Institute for Nanoscale Science & Technology
Ben-Gurion University of the Negev
Beer-Sheva 8410501, Israel
Prof. A. Dubavik
ITMO University
Saint Petersburg 197101, Russia
The ORCID identification number(s) for the author(s) of this article can be found under https://doi.org/10.1002/adom.202000769.

DOI: 10.1002/adom.202000769

nanorod in NIR from ESP, coupled to the waveguide modes, that can switch the overtone excitations 'on' and 'off'.

The hybrid plasmonic–dielectric configuration possesses a unique property: to control the switch with the polarization state of light that allows two different plasmonic modes to co-exist while exciting a single molecular overtone absorption band. Thanks to the possibility of developing energy-efficient, real-time analysis and ultra-compact components at an affordable cost, plasmonics may be the next arrangement in optical communications. Despite the fact that many plasmonics-based applications have appeared, such as sensors,[17] detectors, modulators,[21] switches,[22] and microwave components, no attempts have been made so far in designing all-optical hybrid plasmonic–dielectric switching systems based on the effect of excitation of forbidden molecular overtone transitions. Switches can be classified as all-optical devices, such as optical-to-optical-to-optical (OOO), or optoelectronic such as optical-to-electrical-to-optical (OEO).[23,24] With the help of plasmonic materials, the all-optical switch can be realized in an OOO manner.[25]

Here, we demonstrate the all-optical switch by utilizing two types of plasmons. We excite the ESPs[15,16,26] through the dispersive element prism at the interface between thin metallic (silver) and dielectric films with permittivities of opposite signs. **Figure 1**a,b shows the schematic illustration of a polarized beam incident switch. The state 'on' is activated when the transverse magnetic (TM) polarized light hits the switch; the state 'off' is activated when the transverse electric (TE) polarized beam hits the switch. An additional capability to that of 'on' and 'off' switching is: switching from one channel to another via molecular overtone excitations. As a consequence, it is possible to obtain different field distributions as shown in Figure 1c,d. Here, the main purpose of the switch is to activate the molecules[27] which experience the relaxation time as a response to the continuous wave (CW) on the femtosecond timescale.[28] Here, we report for the first time the time-dependent absorption of the NMA molecules. Time-dependent absorption of other molecules is known and was reported for instance in ref. [29].

2. Results and Discussion

2.1. Coupling Mechanism and Device Performance

Figure 1 illustrates the concept of a real-time, no-energy-consuming, all-optical switch based on molecular excitation under TE and TM polarized light. In state 'on', TM polarized light is being transmitted through the medium in 'S', 'C', and 'L' telecommunications bands, resulting in strong light absorption by molecular overtones, evident from the well-defined peaks. However, in state 'off', TE polarized light fails to excite molecular overtone, therefore a flat optical response to the incident light appears in 'S', 'C,' and 'L' telecommunications bands. The far-field radiation diagrams showing the directivities for each case are discussed in detail later in the Real-Time Switching Control section. At lower wavelengths, however, excited molecular signatures experience different responses to the incident light under TE and TM polarizations. The coupling mechanism of the system is schematically shown in **Figure 2**a and consists of a silicon (Si) film on thin silver (Ag) film placed on the N-SF11 glass substrate. Gold nanorod, embedded in the molecular medium, is placed on the silica (SiO_2) film covering the

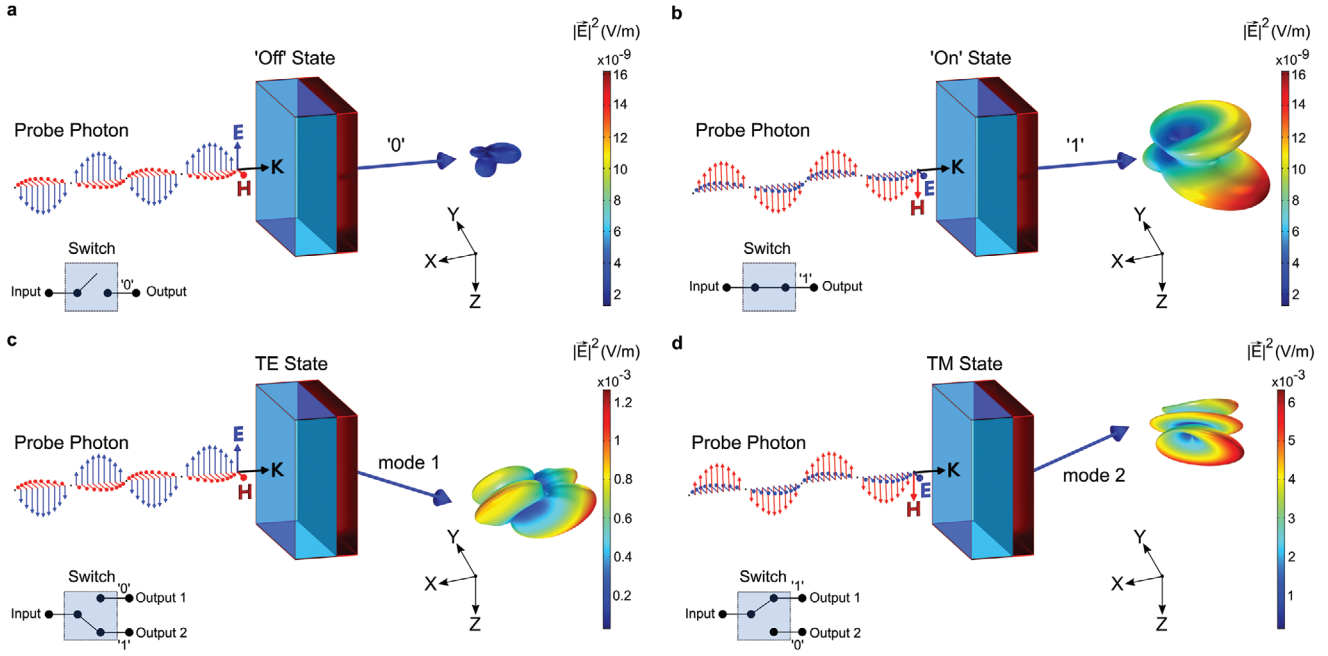

Figure 1. All-optical switch architecture. a) Schematic illustration of polarized incident beam illuminating the switch that operates at optical telecommunication wavelengths through the 'S', 'C', and 'L' bands: the state 'off' is activated when the TE polarized light hits the switch, whereas b) the state 'on' is activated when the TM polarized beam is applied. c) All-optical multiple-switching category in which each mode influences the field distribution resulting in different electric far-field patterns, when TE state operates at around 1100 nm and excites the 2nd N–H overtone, and d) TM state is applied to excite the 1st molecular overtone vibration of the N–H band.

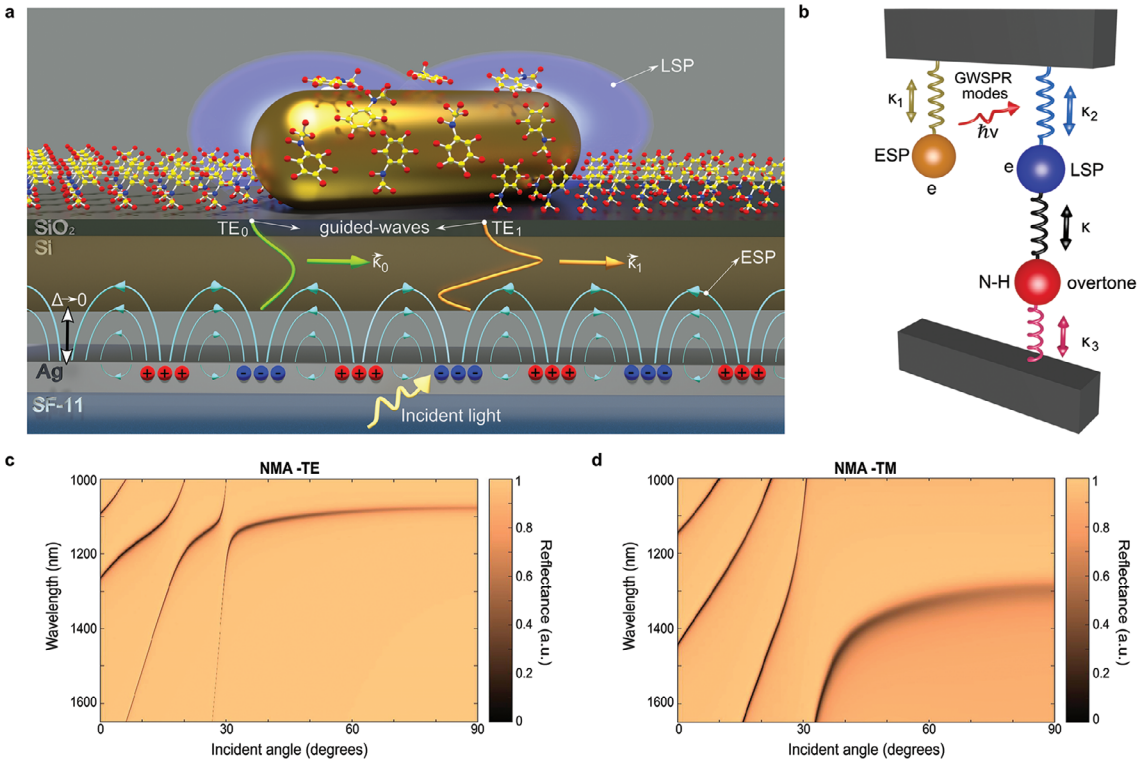

Figure 2. Hybrid plasmonic–dielectric configuration characteristics. a) The coupling mechanism of the hybrid GWSPR-LSPR-overtone system (out of scale, the gap between the Ag and the Si layers is infinitesimally small with $\Delta \to 0$). b) Schematic of the mechanism with three coupled oscillators each at its eigenfrequency, while only oscillator 1 (ESP) is driven by the external force. c,d) Calculated reflectance from multilayer structure consisting of N-SF11 glass substrate covered by 18 nm silver (Ag) under 219 nm silicon film and overlaid by 32 nm of silica (SiO_2) using Abeles-matrix algorithm. Dispersion colormaps of the reflectance in (c) TE and (d) TM polarizations.

silicon. Through the momentum matching condition, the ESP resonance is excited and in turn coupled to the guided modes of the thick silicon film. At the interface between the silica and molecular medium, the guided modes excite the LSP of the gold nanorod. Molecular overtone transitions of N-Methylaniline (NMA) are excited by the LSP of the nanorod. Here we use NMA as a probe molecule with well-defined overtone absorption line in NIR.[1] Figure 2b shows the schematics of the coupling oscillators mechanism. We assigned the oscillator ($i = 1$) to the ESP, oscillator ($i = 2$) to the LSP and oscillator ($i = 3$) to the molecular overtone vibration. We treated the coupling between the ESP to LSP through the guided wave, and from LSP to the overtone as a system with two coupled oscillators with eigenfrequencies $\omega_{i=2,3} = \sqrt{k_i / m_i}$ where k_i and m_i represent the coupling spring constant and mass of i^{th} oscillator by taking into account the anharmonic contribution. The incident time-harmonic field $f(\theta, \lambda, t) = \eta \mathbf{E}(t) = \eta E_0(\theta, \lambda) e^{-i\omega t}$ is generated by the oscillator 1 with a frequency factor η. The coupling mechanism may be explained by the classical equations of motion:[30–32]

$$\ddot{q}_2(t) + \frac{\gamma_2}{m_2}\dot{q}_2(t) + \omega_2^2 q_2(t) + \frac{\kappa}{m_2}\left(q_2(t) - q_3(t)\right) = f(\theta, \lambda, t) \quad (1)$$

$$\ddot{q}_3(t) + \frac{\gamma_3}{m_3}\dot{q}_3(t) + \omega_3^2 q_3(t) + \frac{\kappa}{m_3}\left(q_3(t) - q_2(t)\right) + \frac{\delta}{m_3} q_3^2(t) = 0 \quad (2)$$

where $\gamma_{2,3}$ is the damping coefficients, and δ is the anharmonic coefficient. The oscillators requirement is extremely demanding. To study the coupling mechanism between the ESP and guided-wave surface plasmon resonance (GWSPR) we implemented the Abeles-matrix based algorithm in Matlab and calculated the reflectance of multilayered structure for TE and TM shown in Figure 2c,d in weakly absorbing medium NMA with dispersion as in ref. [31, 33] In Supporting Information, we calculated dispersion maps also for air (n = 1) and water (n = 1.33) as shown in Figure S1, Supporting Information. The guided modes excited in the silicon film are clearly seen when the weakly absorbing medium is considered with a thickness of 1600 nm above the guide. In this work, we show the all-optical switch, engineered to operate at telecommunication wavelengths at the 'S', 'C', and 'L' bands due to the excitation of molecular overtones in hybrid plasmonic–dielectric configuration. This configuration possesses a unique property: to control the switch with the polarization state of light that allows two different plasmonic modes to co-exist while exciting a single overtone absorption band. Controlling the switch is realized by tuning the polarization of incident light from TM to switch-on and TE to switch-off. Using this device, we experimentally demonstrate the real-time optical responses of the switch with a fabricated hybrid plasmonic–dielectric film arrangement. We characterize the switch in a wide spectral range between 1000 and 1650 nm.

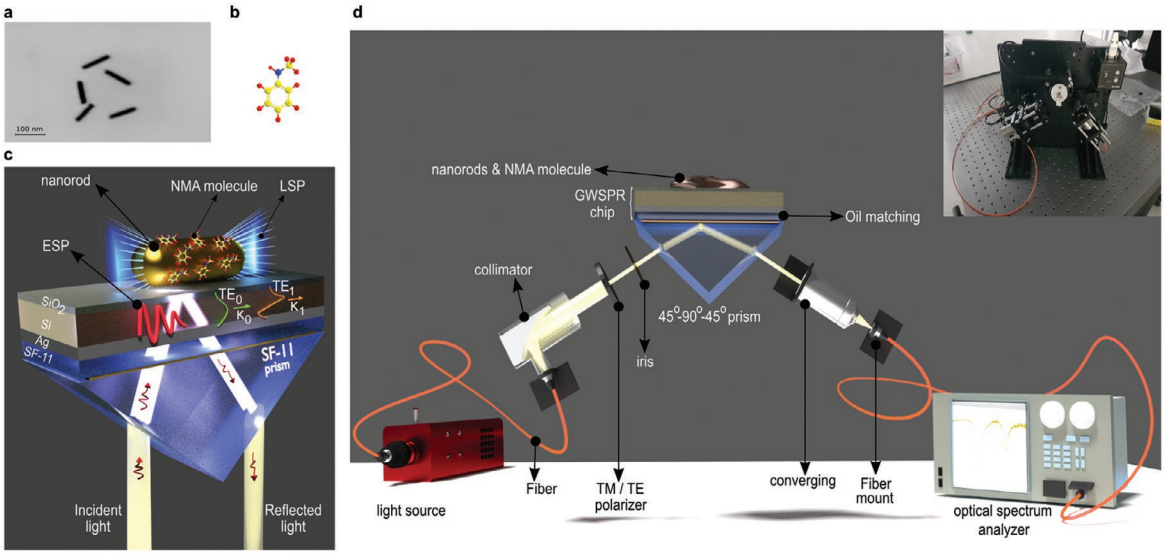

Figure 3. Real-time all-optical polarization-controlled switch experiment. a) Scanning electron micrograph (SEM) of the gold nanorods. b) The molecular structure of NMA. c) Artistic design of the studied system: incident polarized light hits the N-SF11 prism and penetrates the silver–dielectric interface of the thick silicon film and thin SiO_2 film. Gold nanorod is placed on SiO_2 and embedded in NMA. Guided modes are indicated by TE_0 and TE_1 labeling. d) Schematic of the experimental setup: collimated and polarized polychromatic light illuminates the prism facet and is then collected with the focusing objective into the multimode optical fiber, which in turn is connected to the optical spectrum analyzer. The inset shows the photograph of the setup.

2.2. Overtone Transitions in 'S', 'C', and 'L' Bands

We calculated the theoretical guided-wave structure such that the extended plasmonic resonance excites the overtones in 'S', 'C', and 'L' bands. Figure 2c,d shows the calculated dispersion colormaps while varying the wavelengths of interrogation and angle of excitation. The theoretical reflectance shows single TE and TM modes in the guided wave studied structure while the superstrate medium is either air or water. For the water as a superstrate, there is a critical angle of 10° for total internal reflection to occur on the air interface. Calculated reflectance colormaps of TE guided modes for the sample embedded in NMA molecule with a thickness of 1600 nm show interesting landscape with sharp changes associated with the longer lifetime due to the infinite group velocity. Differential reflection shows that the lowest order guided mode vanishes when the sample is embedded in the NMA medium (Figures S1 and S2, Supporting Information).

2.3. Real-Time Switching Control

We fabricated the device, which consists of 219 nm silicon (Si) film on 18 nm silver (Ag) on an N-SF11 glass substrate. Gold nanorod is placed on 32 nm silica (SiO_2) film which is capping the silicon. **Figure 3** shows the experimental setup. The electric fields exponentially decay into both bounding media when the surface plasmon wave propagates along with the metal film-dielectric interface exciting the guided waves of the GWSRP device. The films, composed of silicon on silver, are placed on the prism with matching oil. The weakly absorbing medium consisting of the NMA molecules is dripped onto the surface of the film together with gold nanorods. The thickness of the molecular layer can be controlled by the concentration of the molecule in solvent. Higher concentrations lead to thicker layers as reported in ref. [20] Light hits the base of the prism and penetrates through the thin film while exciting the guided modes. Guided modes of the GWSPR excite the LSPR in which the electromagnetic radiation is localized in the plasmonic nanoparticles, which are much smaller than the wavelength of incident radiation. The energy transfer occurs between the molecular overtone vibrations to the LSPR excited in nanorods. While exploring the orientation of the nanoantenna on the surface of the chip, we noticed the polarization-dependent effect. When the TE polarized incident beam excites the nanoantenna the intensity of absorption cross-section is affected; however, when the TM polarized incident beam excites the nanoantenna, the spectral shift at 'S', 'C', and 'L' bands is observed: **Figure 4**a,b shows time-dependent experimental results with a time interval of $\tau = 1$ s for TE and TM polarized light respectively. The absorption spectra for both TE and TM polarized light experience interesting evolutions with time. One strong peak is observed in Figure 4a which experiences two adjacent resonances. This two adjacent resonances can be explained by the coupling between two nanoantennas oscillators embedded in the NMA medium, as reveal the calculated results shown in Figure 4c. We note, that in the weak coupling regime that the system experiences, the angular frequencies of the oscillators, expressed by ω_2 for LSPR and ω_3 for overtone vibration, are defined by the frequencies equality $\omega_2 = \omega_3 + \Delta\omega$ ($\Delta\omega$ is the spectral distance between the resonant peaks). Figure 4b shows the spectra of two well-defined peaks. The resonance at 1240 nm for TM polarized beam is associated with the excitation of the guided mode of GWSPR configuration, as can be seen from the dispersion map in Figure 2d. The resonance at 'S', 'C', and 'L' bands experiences the redshift with time and is associated with the coupling between LSP to molecular overtones. The temporal dynamic of this resonance is explained by the time-dependent absorption of the molecule at the nanorod surface and therefore the

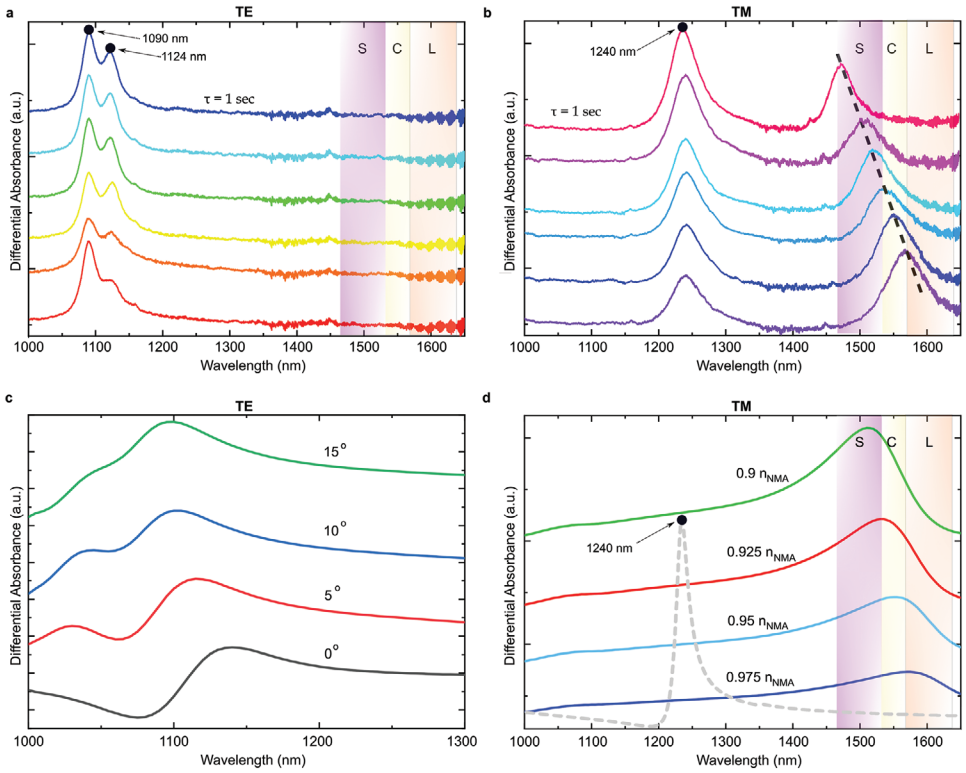

Figure 4. Experimental evidence of plasmonic influence on the molecular overtone absorption. Measured differential absorbance spectra of the gold nanorods embedded in weakly absorbing medium on the GWSPR sample, showing: a) switch-off, TE polarized light fails to excite molecular overtone, therefore a flat optical response to the incident light appears in 'S', 'C' and 'L' bands; and b) switch-on, TM polarized light is being transmitted through the medium, resulting in strong light absorption by molecular overtones, evident from the well-defined peaks in 'S', 'C', and 'L' bands. The 'S', 'C', and 'L' bands are highlighted in transparent boxes. The time interval between the signals is $\tau = 1$ s for two orthogonal polarizations TE and TM. The top curves, blue in (a) for TE and red in (b) for TM, represent the optical signals at 0 s. Multiple switching is applied on different wavelength regions showing that a) the two adjacent resonances appear when TE state is activated, and b) when TM state is activated the resonance experiences the redshift. c,d) Numerical simulation results of differential absorbance spectra of the gold nanorods positioned on the silica layers and embedded in infinite NMA medium. Each curve in (c) represents a different angle from 0° to 15° between the nanorods along the *x*-axis for TE polarization. In (d), for TM polarization, each curve is associated with different effective index $n_{\text{eff}} = a \cdot n_{\text{NMA}}$ from $a = 0.9$ to $a = 0.975$. Grey dashed line was numerically calculated and is associated with the GWSPR mode at 1240 nm.

time-dependent effective refractive index $n_{eff} = n(t)$ (fraction of the molecule in air). This remarkable result indicates that one can tune the resonance wavelength by adjusting the refractive index of the molecule, as shown in Figure 4d. To better understand the polarization controlled switching of the medium, it is necessary to analyze the behavior of the electric far-field scattering effect. **Figure 5**a shows the calculated electric far-field component directivities when the system is illuminated by TM (top) or TE (bottom) polarized incident beam. When the system is illuminated by the TE polarized light, the far-field radiation pattern is extremely small which is a signature of switch-off behavior of the device (Figure 5b, bottom). However, when the system is illuminated by the TM polarized light, the strong directivity of the major lobe scattering effect is revealed (Figure 5b, top). The width of the major lobe depends on the number of elements that act as an array in the medium; generally, it becomes narrower when the number of elements is increased.[34,35] In contrast, at lower wavelengths, bifurcated side-scattering appears for TE incident light while circular top-bottom radiation pattern appears when the illumination is TM, as presented in the radiation pattern in Figure 1c,d. Figure 5c shows the polar radiation pattern for 'on' state (top) and for 'off' state (bottom). A main significant lobe occurs in the negative *x*-axis direction, where maximum radiation is present, while the minor secondary lobes experience losses. We note that the scattered lobe in 'on' state is of a higher order of magnitude than that in the 'off' state. The radiation pattern of the nanoantennas appears to exhibit an endfire-like radiation shape. This unidirectional radiation may be explained by a phase difference between the currents of each nanorod but with the same magnitudes.[36,37] However, in this arrangement, the radiated energy gets diverted to the negative *x*-axis direction. This allows avoidance of the minor lobes and, in consequence, an increase in the directivity.

3. Conclusion

In summary, we demonstrated real-time all-optical sensor-switch involving polarization-dependent molecular overtone transitions, which represents the most efficient photomolecular sensor device to date. Despite the relatively low oscillator strength of the corresponding forbidden dipole transition in

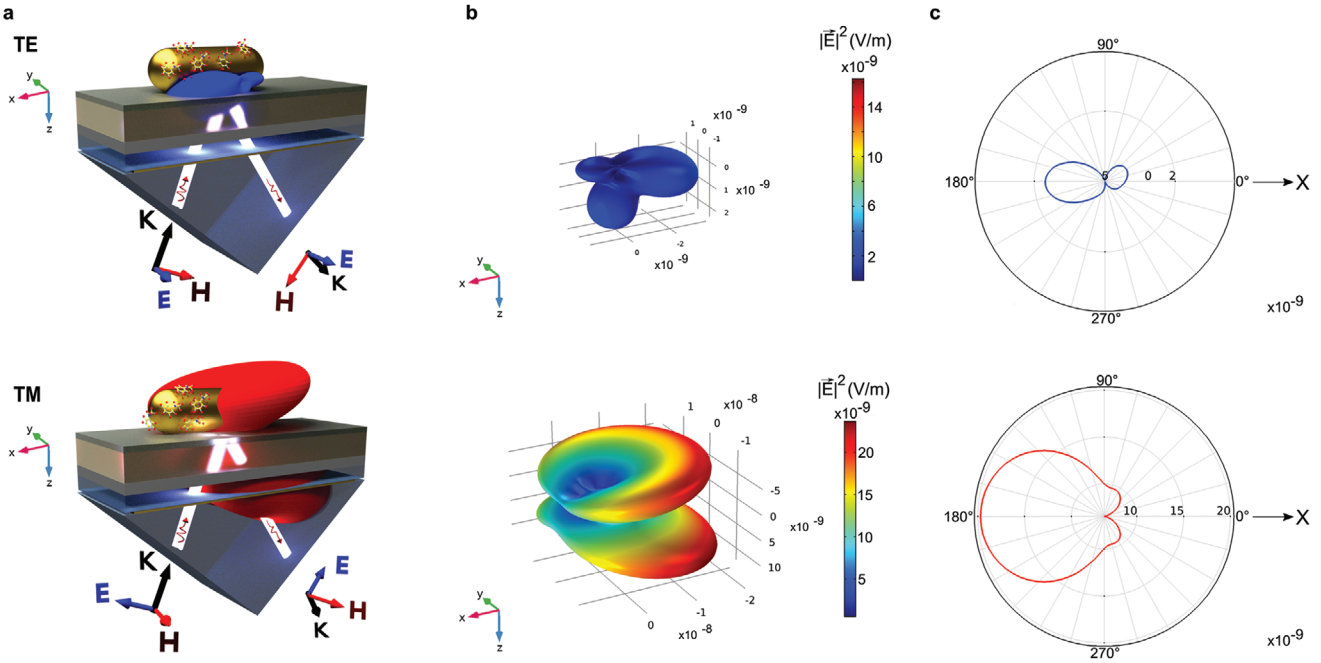

Figure 5. Far-field radiation patterns. a) Schematic of the system with polarization-dependent far-field radiation diagram from gold nanorod along the *x*-axis while the nanorod is embedded in weakly NMA absorbing medium for TE (top) and TM (bottom); the direction of the incident light is indicated by the *k* vector. b) Calculated far-field directivities of electric field at 1500 nm when the system is illuminated by TE (top) or TM (bottom) polarized incident light. c) 2D patterns of the far-field radiation when the normal is in the *xz*-plane and the reference direction is on the *x*-axis for "off" (top) and "on" (bottom) switching.

harmonic oscillator approximation, we constructed an optical switching system based on polarization-dependent properties of the plasmon-to-overtone coupled modes. This all-optical sensor-switch manifold is realized by excited localized surface plasmons which couple to the overtones molecular vibrations. We revealed the critical role of the hybrid-plasmonic nature of the device in tuning the sensor-switch, so the molecular overtone transitions are excited via LSPR of the nanorod. LSPR of the nanorod is in turn, excited by the ESP through the guided modes of the silicon-based guided-wave SPR (GWSPR). The engineered sensor indicates a unique opportunity for the novel type of efficient sensor-switches based on the guided-wave plasmonic structure that we fabricated, characterized and tested experimentally. We synthesized gold nanoparticles and showed the efficient energy transfer between the overtone vibration and plasmonic nanoparticles. Our findings show that the overtone excitations can be switched simply by changing the polarization of the incident beam. Our discovery opens new avenues of chip-scale polarization activated organic sensors compatible with the silicon photonics platform.

4. Experimental Section

Materials: *N*-methylaniline (NMA, $C_6H_5NH(CH_3)$, ≥98%) and the matching oils (with refractive indexes of 1.74 and 1.57) were purchased from Sigma-Aldrich. Amorphous silicon (Si), and silicon dioxide (SiO_2, purity of 99.99%) purchased from Kurt J. Lesker were deposited. The silver (Ag, purity of 99.99%) was purchased from Holland Moran. Chemicals for nanorods synthesis: all chemicals were obtained from commercial suppliers and used without further purification. Cetyltrimethylammonium bromide (CTAB, ≥98.0%), hydrogen tetrachloroaurate trihydrate ($HAuCl_4 \cdot 3H_2O$, ≥99.9%), L-ascorbic acid (reagent grade), silver nitrate ($AgNO_3$, 99.9999%), sodium borohydride ($NaBH_4$, 99.99%) were purchased from Sigma Aldrich. Oleic acid was purchased from Fisher Scientific. Sodium hydroxide from Solvay (France). Methoxy-Poly (Ethyleneglycol)-Thiol (mPEG-SH, MW 350) was synthesized according to ref. [38]. Hydrochloric acid (HCl, 37 wt% in water) was purchased from Vekton (Russia). Ultrapure water obtained from a Hydrolab HLP Smart system was used in all experiments. All glassware was cleaned using freshly prepared aqua regia ($HCl:HNO_3$ in a 3:1 ratio by volume) and rinsed by deionized water.

Numerical Simulation and Calculations: The code for dispersion relations was implemented in Matlab environment, as well as the reflectivity of GWSPR configuration which was calculated based on the Abeles matrix method as a function of wavelength and incident angle. For far-field radiation patterns of the electric field and absorption cross-sections of nanorods, the three-dimensional simulation was performed using a commercial COMSOL Multiphysics 5.4 software based on the finite element analysis method in wave optics module, as a unit cell with periodic boundary condition. Mesh was explored to ensure the accuracy of the calculated results. The empirical dielectric functions of the silicon and silica were taken from the Refractive-Index database (https://refractiveindex.info). In the simulation, the collection of gold nanorods oriented at different angles from 0° to 15° was considered. All with a length of 100 nm and a diameter of 10.5 nm as measured by SEM of the fabricated nanorods. The description of the simulation and calculations is detailed in the Supporting Information.

GWSPR Fabrication: Prior to the fabrication, the N-SF11 glass substrate was solvent cleaned with piranha cleaning (a mixture of sulfuric acid H_2SO_4 with hydrogen peroxide H_2O_2, 3:1 by volume) for 10 min, and then the substrate was washed with water. Three layers were sequentially e-beam evaporated on the N-SF11 glass substrate by E-GUN VST system under a base pressure of ~4×10^{-6} Torr. First, silver (Ag) with a density of 10.5 gm·cc^{-1} evaporated on the substrate to create an 18 nm film. Next, 219 nm silicon (Si) film was deposited with 7.2 gm·cc^{-1}

density. Finally, 32 nm silicon dioxide (SiO_2) film with 2.2 gm·cc^{-1} density was deposited.

Samples Characterization: The thickness of the GWSPR fabricated sample was measured with Stylus profilometer, Veeco Dektak-8. To verify the accuracy of our fabrication process, the thickness of the sample was examined and spectrum analysis was performed with J.A. Woollam spectroscopic, alpha-SE ellipsometer.

Nanorods Synthesis: Sodium oleate was obtained by adding sodium hydroxide (1.42 g, 35.2 mmol) to oleic acid (11.12 mL, 35.2 mmol) dissolved in 100 mL of 70% ethanol. The reaction mixture was stirred overnight at room temperature. The solvent was removed by rotary evaporation, resulting in the product as a white soap. Synthesis of Gold nanorods consists of two steps: 1) Au seed solution for nanorod growth was prepared as follows: 5 mL of 0.5 mM $HAuCl_4$ was mixed with 5 mL of 0.2 M CTAB solution in a 10 mL plastic vial. 0.6 mL of freshly prepared 0.01M $NaBH_4$ was diluted to 1.0 mL with water and was then injected into the Au(III)-CTAB solution under vigorous stirring (approximately 1200 rpm). The solution color changed from yellow to brownish tone. Stirring was terminated after 2 min and the solution aged at room temperature for 30 min before use. 2) To prepare the Au nanorod solution, 3.5 g (0.047 M in the final growth solution) of CTAB and 0.6 g of sodium oleate were dissolved in 125 mL of warm water (~50 °C) in a 250 mL flask. The solution was cooled down to 30 °C and 12 mL of 4 mM $AgNO_3$ solution was added. The mixture was kept undisturbed at 30 °C for 15 min after which 125 mL of 1 mM $HAuCl_4$ solution was added. The solution became colorless after 90 min of stirring (approximately 700 rpm) and 1.5 mL of HCl (37 wt% in water) was injected to adjust the pH accordingly. After another 15 min of slow stirring at approximately 400 rpm, 0.625 mL of 0.064 M ascorbic acid was added and the solution was vigorously stirred for 30 s. Finally, a 0.2 mL of Au seed solution was injected into the growth solution. The resultant mixture was stirred for 30 s and left undisturbed at 30 °C for 12 h for nanorod growth. Ligand exchange using mPEG-SH: 15 mL of the prepared solution was centrifuged for 10 min at 7000 rpm. The supernatant was removed from the final precipitated Au nanorods. Au nanorods were mixed with 0.5 mL aqueous mPEG-SH solution (10 mg·mL^{-1}) and sonicated for 1-2 min. The solution obtained was centrifuged again for 10 min at 7000 rpm. The addition of aqueous thiolated PEG solution to Au nanorods and sonication was repeated one more time. The final water solution was mixed with chloroform until the Au nanorods transferred to the organic layer.

Nanorods Characterization: The physical dimensions of the gold nanorods and their shape were analyzed by scanning electron microscopy (SEM) using Merlin (Carl Zeiss) as shown in Figure 3a.

Experimental Setup: The stabilized fiber-coupled light source (SLS201L), bandwidth from 360 to 2600 nm, was collimated into the prism using a protected silver reflective collimator (RC04FC-P01, 450 nm-20 µm, ∅4 mm beam). Polarized (WP25M-UB, ∅25 mm mounted wire grid polarizer, 250 nm to 4 µm) collimated light passes through the iris. To allow flexibility in determining the angle of the incident light, the N-SF11 micro right-angle prism (15 mm, uncoated, purchased from Edmund optics) was positioned on a motorized rotary stage system (Zaber™) with an accuracy of 0.1°. The reflected light focused into fiber using an × 4 plan achromat objective (Olympus, RMS4X) with a numerical aperture of $NA = 0.1$, to collect the spectra directly into the optical spectrum analyzer (Yokogawa 6370D). Next, the fabricated sample was placed on the base of the prism and dripped the matching oil between the sample and the prism. The nanorods were placed on the sample. Finally, the analytic material was dripped on the nanorods.

Optical System Calibration: Since the e-beam evaporation process affects the fabricated sample, the system was calibrated by measuring the known reflectance in air and compared this to the calculated results (see Figure S3, Supporting Information). For the ultrathin silver film, the optical constant changes regularly as the silver film thickness decrease.[39,40] Modifications were implemented to distributions of n and k of the refractive index for silver and silicon films (shown in Figure S4, Supporting Information).

Absorption Spectra Calculations: To estimate the absorption of the nanorods with the NMA molecule, Maxwell's equations were solved numerically. First, the simulation computes a background field from the incident light to GWSPR configuration, followed by the total field with the nanorod present which allows us to plot the absorption cross-section via the power loss density in the nanorod. To quantify the absorption of the nanorod and NMA molecule overtones, the differential absorption was calculated:[41–43]

$$\Delta A(\lambda) = \frac{A_{\text{mol}}}{A_{\text{BG}}} = \sigma_{\text{abs}}\left(\text{NR}|_{\text{Au}(\lambda)} + \text{NMA}|_{n(\lambda)}\right)\Big|_{dB} - \sigma_{\text{abs}}\left(\text{NR}|_{\text{Au}(\lambda)} + \text{oil}\|_{n=1.57}\right)\Big|_{dB} \quad (3)$$

Here, A_{mol} is the absorption when the nanorod is embedded in the molecule, whereas A_{BG} is the absorption of the background (the matching oil with the background refractive index).

Spectroscopy Measurements: For the reflectance spectrum of the coupled three-resonator system, the intensity of the reflected beam when the NMA molecule is present on the nanorods was first measured. As the reference measurement, the spectra when the sample was immersed in the matching oil with a refractive index of 1.57 (corresponding to the real part of the complex refractive index) was collected. The cross-section of the differential reflection was then plotted, which is defined as:[41–43]

$$\Delta R(\lambda) = \frac{|\Gamma_{\text{NMA}}|^2}{|\Gamma_{\text{oil}}|^2} \quad (4)$$

Here, $|\Gamma_{\text{NMA}}|^2$ is the reflectance when the nanorod was embedded in the molecule, whereas $|\Gamma_{\text{oil}}|^2$ is the reflectance of the background (when the nanorod was embedded in the matching oil). The measurements were performed for both TE and TM polarized light. For all cases, the incident angle was fixed to 28.7°. In each case, six samples were sampled to follow the changes as a function of time.

Supporting Information

Supporting Information is available from the Wiley Online Library or from the author.

Acknowledgements

The authors acknowledge the financial support from the Israel Innovation Authority Kamin Program (Grant no. 69073). A.H. acknowledges the scholarship of KLA. The authors acknowledge Benny Hadad for assistance in device fabrication and Marat Spector for fruitful discussions. A.D. acknowledges Aleksander P. Litvin (ITMO University) for the characterization of the nanorods and Mikhail Baranov for the SEM measurements. A.D. acknowledges the Russian Science Foundation (Grant no. 19-13-00332) for financial support.

Conflict of Interest

The authors declare no conflict of interest.

Keywords

hybrid optical materials, molecular overtones, nanophotonics, near-infrared spectroscopy, optical switches, surface plasmon resonance, waveguides

Received: May 10, 2020
Revised: June 29, 2020
Published online:

[1] A. Karbchevsky, A. Katiyi, A. S. Ang, A. Hazan, *Nanophotonics* **2020**, https://doi.org/10.1515/nanoph-2020-0204.
[2] J. E. Midwinter, *Nature* **1976**, *261*, 371.
[3] B. E. A. Saleh, M. C. Teich, *Fundamentals of Photonics*, John Wiley & Sons, Hoboken, NJ **2019**.
[4] J. E. Midwinter, in *Photonic Switching* (Eds: T. K. Gustafson, P. W. Smith), Springer Series in Electronics and Photonics, volume 25, Springer-Verlag, Berlin, Heidelberg **1988**, pp. 14–23.
[5] Z. Sun, D. W. Snoke, *Nat. Photonics* **2019**, *13*, 370.
[6] L. Hou, X. Zhang, G. F. Cotella, G. Carnicella, M. Herder, B. M. Schmidt, M. Pätzel, S. Hecht, F. Cacialli, P. Samorì, *Nat. Nanotechnol.* **2019**, *14*, 347.
[7] K. Nozaki, T. Tanabe, A. Shinya, S. Matsuo, T. Sato, H. Taniyama, M. Notomi, *Nat. Photonics* **2010**, *4*, 477.
[8] M. Sun, M. Taha, S. Walia, M. Bhaskaran, S. Sriram, W. Shieh, R. R. Unnithan, *Sci. Rep.* **2018**, *8*, 11106.
[9] S. Manz, M. Matsubara, T. Lottermoser, J. Büchi, A. Iyama, T. Kimura, D. Meier, M. Fiebig, *Nat. Photonics* **2016**, *10*, 653.
[10] Y. Yang, K. Kelley, E. Sachet, S. Campione, T. S. Luk, J. P. Maria, M. B. Sinclair, I. Brener, *Nat. Photonics* **2017**, *11*, 390.
[11] D. T. Payne, W. A. Webre, Y. Matsushita, N. Zhu, Z. Futera, J. Labuta, W. Jevasuwan, N. Fukata, J. S. Fossey, F. D'Souza, K. Ariga, W. Schmitt, J. P. Hill, *Nat. Commun.* **2019**, *10*, 1007.
[12] J. Tian, H. Luo, Y. Yang, F. Ding, Y. Qu, D. Zhao, M. Qiu, S. I. Bozhevolnyi, *Nat. Commun.* **2019**, *10*, 396.
[13] M. Ono, M. Hata, M. Tsunekawa, K. Nozaki, H. Sumikura, H. Chiba, M. Notomi, *Nat. Photonics* **2020**, *14*, 37.
[14] G. X. Ni, L. Wang, M. D. Goldflam, M. Wagner, Z. Fei, A. S. McLeod, M. K. Liu, F. Keilmann, B. Özyilmaz, A. H. Castro Neto, J. Hone, M. M. Fogler, D. N. Basov, *Nat. Photonics* **2016**, *10*, 244.
[15] W. L. Barnes, A. Dereux, T. W. Ebbesen, *Nature* **2003**, *424*, 824.
[16] A. Karabchevsky, S. Karabchevsky, I. Abdulhalim, *Sens. Actuators B, Chem.* **2011**, *155*, 361.
[17] A. Karabchevsky, A. Mosayyebi, A. V. Kavokin, *Light Sci. Appl.* **2016**, *5*, e16164.
[18] A. Katiyi, A. Karabchevsky, *ACS Sens.* **2018**, *3*, 618.
[19] A. Karabchevsky, A. Katiyi, M. I. M. Bin Abdul Khudus, A. V. Kavokin, *ACS Photonics* **2018**, *5*, 2200.
[20] A. Karabchevsky, A. V. Kavokin, *Sci. Rep.* **2016**, *6*, 21201.
[21] A. Smolyaninov, A. El Amili, F. Vallini, S. Pappert, Y. Fainman, *Nat. Photonics* **2019**, *13*, 431.
[22] L. H. Nicholls, F. J. Rodríguez-Fortuño, M. E. Nasir, R. M. Córdova-Castro, N. Olivier, G. A. Wurtz, A. V. Zayats, *Nat. Photonics* **2017**, *11*, 628.
[23] T. Nikolajsen, K. Leosson, S. I. Bozhevolnyi, *Appl. Phys. Lett.* **2004**, *85*, 5833.
[24] K. Nozaki, S. Matsuo, T. Fujii, K. Takeda, A. Shinya, E. Kuramochi, M. Notomi, *Nat. Photonics* **2019**, *13*, 454.
[25] Z. Pan, P. Lang, G. Duan, *Mod. Phys. Lett. B* **2018**, *32*, 1850134.
[26] D. K. Gramotnev, S. I. Bozhevolnyi, *Nat. Photonics* **2010**, *4*, 83.
[27] F. Kurtz, C. Ropers, G. Herink, *Nat. Photonics* **2019**, *14*, 9.
[28] J. Tan, J. Zhang, C. Li, Y. Luo, S. Ye, *Nat. Commun.* **2019**, *10*, 1010.
[29] D. R. Nascimento, A. E. DePrince III, *J. Chem. Theory Comput.* **2016**, *12*, 5834.
[30] M. Zhao, H. Li, Z. He, Z. Chen, H. Xu, M. Zheng, *Sci. Rep.* **2017**, *7*, 10635.
[31] C. L. Garrido Alzar, M. A. G. Martinez, P. Nussenzveig, *Am. J. Phys.* **2002**, *70*, 37.
[32] J. M. Hollas, *Modern Spectroscopy*, 4th ed., John Wiley & Sons, Chichester, UK **2004**.
[33] A. Katiyi, A. Karabchevsky, *J. Light. Technol.* **2017**, *35*, 2902.
[34] A. E. Krasnok, I. S. Maksymov, A. I. Denisyuk, P. A. Belov, A. E. Miroshnichenko, C. R. Simovski, Y. S. Kivshar, *Physics-Uspekhi* **2013**, *56*, 539.
[35] J. Li, Ph.D. thesis, University of Pennsylvania **2007**.
[36] T. Pakizeh, M. Käll, *Nano Lett.* **2009**, *9*, 2343.
[37] X. X. Liu, A. Alù, *Phys. Rev. B* **2010**, *82*, 144305.
[38] A. Dubavik, V. Lesnyak, W. Thiessen, N. Gaponik, T. Wolff, A. Eychmüller, *J. Phys. Chem. C* **2009**, *113*, 4748.
[39] Z. Ming, L. Yao Peng, Z. Sheng, L. Ding Quan, *Chin. Phys. Lett.* **2015**, *32*, 77802.
[40] G. Ding, C. Clavero, D. Schweigert, M. Le, *AIP Adv.* **2015**, *5*, 117234.
[41] A. Karabchevsky, A. Shalabney, in *Proc. Optical Sensing and Detection IV*, SPIE, **2016**, *9899*, 98991T.
[42] D. R. Dadadzhanov, T. A. Vartanyan, A. Karabchevsky, *Opt. Express* **2019**, *27*, 29471.
[43] D. R. Dadadzhanov, T. A. Vartanyan, A. Karabchevsky, *Nanomaterials* **2020**, *10*, 1265.

